



Grain boundary engineering for enhancing intergranular damage resistance of ferritic/martensitic steel P92

Lei Peng^{1,2} · Shang-Ming Chen^{1,2} · Jing-Yi Shi^{1,2} · Yong-Jie Sun^{1,2} · Yi-Fei Liu^{1,2} · Yin-Zhong Shen³ · Hong-Ya He³ · Hui-Juan Wang⁴ · Jie Tian⁴

Received: 31 May 2023 / Revised: 10 October 2023 / Accepted: 16 October 2023 / Published online: 9 April 2024

© The Author(s), under exclusive licence to China Science Publishing & Media Ltd. (Science Press), Shanghai Institute of Applied Physics, the Chinese Academy of Sciences, Chinese Nuclear Society 2024

Abstract

Ferritic/martensitic (F/M) steel is widely used as a structural material in thermal and nuclear power plants. However, it is susceptible to intergranular damage, which is a critical issue, under service conditions. In this study, to improve the resistance to intergranular damage of F/M steel, a thermomechanical process (TMP) was employed to achieve a grain boundary engineering (GBE) microstructure in F/M steel P92. The TMP, including cold-rolling thickness reduction of 6%, 9%, and 12%, followed by austenitization at 1323 K for 40 min and tempering at 1053 K for 45 min, was applied to the as-received (AR) P92 steel. The prior austenite grain (PAG) size, prior austenite grain boundary character distribution (GBCD), and connectivity of prior austenite grain boundaries (PAGBs) were investigated. Compared to the AR specimen, the PAG size did not change significantly. The fraction of coincident site lattice boundaries (CSLBs, $3 \leq \Sigma \leq 29$) and $\Sigma 3^n$ boundaries along PAGBs decreased with increasing reduction ratio because the recrystallization fraction increased with increasing reduction ratio. The PAGB connectivity of the 6% deformed specimen slightly deteriorated compared with that of the AR specimen. Moreover, potentiodynamic polarization studies revealed that the intergranular damage resistance of the studied steel could be improved by increasing the fraction of CSLBs along the PAGBs, indicating that the TMP, which involves low deformation, could enhance the intergranular damage resistance.

Keywords Grain boundary engineering · Ferritic/martensitic steel · Prior austenite grain boundary character distribution · Grain boundary connectivity · Intergranular damage resistance

1 Introduction

Ferritic/martensitic (F/M) steels have been widely used as structural materials in thermal and nuclear power plants [1–3] and are candidate fuel cladding materials in advanced Gen-IV reactors [4–6] because they have higher thermal conductivity, lower cost, and greater resistance to radiation-induced void swelling than austenitic stainless steels [7]. As an advanced F/M steel, the P92 steel is microalloyed with vanadium and niobium, and its boron and nitrogen contents

are controlled. Owing to the higher temperature strength and better creep properties of P92 steel compared to those of other F/M steels [8–10], it has been used or considered for preferential use in thermal and nuclear power plant components (e.g., main steam pipes, reheat steam pipes, boilers, and turbines). However, relevant studies have shown that a high-temperature steam environment and some components of salt accumulation can accelerate the corrosion of steam pipelines and even cause pipe bursts. Therefore, it is of great significance to improve the intergranular corrosion resistance of P92 steel.

Previous studies [11, 12] have revealed that sensitization, that is, chromium depletion due to chromium carbide precipitation at the grain boundaries (GBs), results in the degradation of intergranular corrosion resistance. Zhou et al. [13] and Randle et al. [14] reported that special GBs, that is, coincident site lattice boundaries (CSLBs), strongly suppress chromium carbide precipitation. Therefore, it is

This work was supported by the National Natural Science Foundation of China (Nos. 12175231 and 11805131), Anhui Natural Science Foundation of China (No. 2108085J05), Projects of International Cooperation and Exchanges NSFC (No. 51111140389), and the Collaborative Innovation Program of the Hefei Science Center, CAS (Nos. 2021HSC-CIP020 and 2022HSC-CIP009).

Extended author information available on the last page of the article

believed that grain boundary engineering (GBE) [11, 15] is an economical and effective solution for improving the resistance to chromium depletion and suppressing the formation of carbide precipitates along GBs by introducing CSLBs. In F/M steels, prior austenite grain boundaries (PAGBs) behave as preferential sites for intergranular corrosion [16]. Thus, previous studies [16–18] have reported that an increase in the fraction of CSLBs ($3 \leq \Sigma \leq 29$) along PAGBs can enhance the intergranular corrosion resistance of F/M steel. GBE, which involves a series of thermomechanical processes (TMPs), can improve the grain boundary character distribution (GBCD) and disrupt random boundaries without disturbing the original microstructure by increasing the fraction of CSLBs along the PAGBs. In recent decades, GBE has been successfully applied to several nickel-based alloys [19–21] and austenitic steels [22–24]. Based on the abovementioned successful applications, researchers have attempted to introduce the GBE method for the modification of F/M steel. To the best of our knowledge, it is believed that a TMP can effectively achieve a GBE microstructure in a metal material [19, 25–29] with a low stacking fault energy (SFE). However, few studies [17, 29] have used a TMP to study the prior austenite GBCD in F/M steel because materials with bcc structures have a higher SFE than materials with fcc structures, and the mechanism of GB evolution and transformation of F/M steel is not clear and requires systematic analysis. Therefore, it was necessary to use the GBE method to study the effects of different TMPs on PAGBs.

The electrochemical corrosion test is an important method for investigating the corrosion resistance of materials and has been shown to be environmentally friendly, economical, nondestructive, quantitative, and useful [30–32] for corrosion studies in laboratory investigations. In the last decade, a significant amount of research on the corrosion behavior of 304 stainless steel [12], rusted steel [32], EH47 ship steel [33], and titanium-clad carbon steel [34] has been successfully conducted utilizing electrochemical corrosion tests. Thus, electrochemical techniques can provide a basis for evaluating the corrosion resistance of the studied specimens.

The purpose of this study was to evaluate the effects of different deformations on P92 steel. Prior austenite grain (PAG) size, prior austenite GBCD, PAGB connectivity, and carbide particles were investigated via metallographic analysis and scanning electron microscopy (SEM)/electron backscatter diffraction (EBSD). Corrosion tests were conducted to verify the feasibility of improving the corrosion resistance. The corrosion performance of P92 steel in 0.03 M Na₂SO₄ and 0.03 M NaCl aqueous solutions [35] was determined through potentiodynamic polarization tests. The results are expected to provide insights into

methods to enhance the intergranular damage resistance of P92 steel.

2 Material and method

2.1 Experimental material

A commercial F/M steel P92 pipe with a wall thickness of 60 mm without service was selected as the initial material in this study, and its mechanical properties were reported in Refs. [36–42]. The pipe was delivered after a final heat treatment consisting of normalizing and tempering (NT). Normalizing was conducted at 1323 K for 30 min, whereas tempering was conducted at 1038 K for 60 min. After NT, the pipe was cooled to room temperature. The chemical composition of the pipe was 0.093 C, 0.14 Si, 0.41 Mn, 8.75 Cr, 1.62 W, 0.183 V, 0.052 Nb, 0.063 N, 0.207 Ni, 0.505 Mo, 0.001 Ti, 0.003 B (wt%), and bare Fe. Previous studies [17, 43] suggested that strain-induced boundary migration (SIBM) can improve the fraction and distribution of CSLBs along the PAGB. Consequently, steel plates with dimensions of 300 mm × 60 mm × 2.5 mm were subjected to a TMP involving three cold-rolling reduction ratios, namely, 6%, 9%, and 12%, followed by austenitization at 1323 K for 40 min, tempering at 1053 K for 45 min, and air cooling. Figure 1 shows the TMP routes for all the specimens. The as-received and 6%, 9%, and 12% deformed specimens are designated as AR, 6D, 9D, and 12D, respectively. The nomenclature of each specimen is listed in Table 1. The specimens were cut normal to the rolling direction to observe the microstructure; the observation area was located at the edge of the specimen.

2.2 Microstructural investigation

Specimens for EBSD analyses with a dimension of 10 mm × 10 mm × (2.2–2.35) mm were cut from the inside TMP-treated steel plates, and the EBSD scanning area was vertical to the plate surface. The specimens were first mechanically ground with SiC paper in different grits, up to 5000 grit, and then mechanically polished with a diamond solution with different diamond grain sizes, up to 1 μm. The final polishing was carried out with 0.04 μm silica solution. The GB was quantitatively evaluated using a ZEISS Gemini SEM 500 scanning electron microscope equipped with a Nordlys Max3 EBSD probe. The acceleration voltage was 20 kV, the beam current was 10 μA, and the scanning step size was 0.09–0.2 μm. The work adopted Brandon's criterion to categorize the CSLBs: $\Delta\theta \leq 15^\circ \Sigma^{-1/2}$ [44], and boundaries with $2^\circ \leq \theta < 10^\circ$ were considered as low angle grain boundaries (LAGBs). After EBSD scanning, Aztec crystal 2.1 software was used to reconstruct the PAG, assuming

Fig. 1 (Color online) Schematic representation of thermomechanical processing of P92 steel

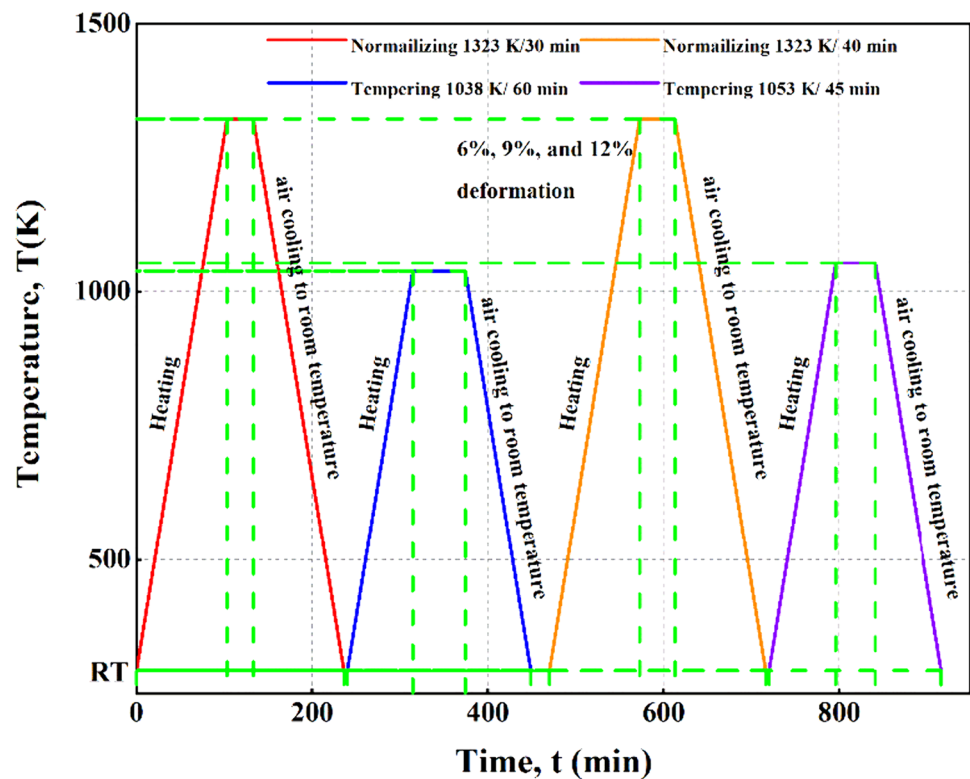


Table 1 Nomenclature of the thermomechanically treated specimens used in this work

Reduction ratio (%)	Normalizing tempering (K)	Normalizing time (min)	Tempering temperature (K)	Tempering time (min)	Specimen nomenclature
–	–	–	–	–	AR
6	1323	40	1053	45	6D
9	1323	40	1053	45	9D
12	1323	40	1053	45	12D

a Kurdjumov–Sachs (K–S) orientation relationship [29, 45–48]. Aztec crystal 2.1 software was used for subsequent analyses.

The EBSD maps of the AR specimens are shown in Fig. 2. The maps were cropped to $100\ \mu\text{m} \times 50\ \mu\text{m}$ for better visualization of the microstructure. A typical lath-martensite microstructure is shown in Fig. 2. The inverse pole figure (IPF) maps of AR specimen after the PAG reconstruction was shown in Fig. 2, it can be clearly observed that the martensite lath disappears and PAGBs appear during the process of PAG reconstruction. The reconstructed PAG size is $\sim 20\ \mu\text{m}$, which is similar to the metallographic result and the result obtained by T. Sakthivel et al. [49]. Relevant statistical results will be analyzed in the following sections.

Compared with the EBSD technique, metallographic analysis can observe a larger area, which can ensure the accuracy of the PAG size measurement. In the metallographic method used to reveal the microstructure, the

specimens were ground, polished, and etched in a solution of 1.5 mL nitric acid (superiorly pure), 1 mL hydrofluoric acid (analytically pure), 2 mL hydrogen peroxide (30%, analytically pure), 10 mL detergent (including surfactant), and 50 mL distilled water for 2–10 s. The linear intercept method was used to measure the PAG size from the metallographic images. All images showed more than 500 PAGs and more than 30 lines were randomly drawn on each image.

2.3 Corrosion test

Electrochemical corrosion tests were performed to study the effect of the TMP on intergranular damage resistance. To perform the electrochemical corrosion test, the specimen was wire cut to a size of $10\ \text{mm} \times 2\ \text{mm} \times (2.2\text{--}2.35)\ \text{mm}$. The electrochemical specimen was welded to a copper conductor and sealed with epoxy resin, such that the exposed working surface area was $0.22\text{--}0.235\ \text{cm}^2$. The surfaces

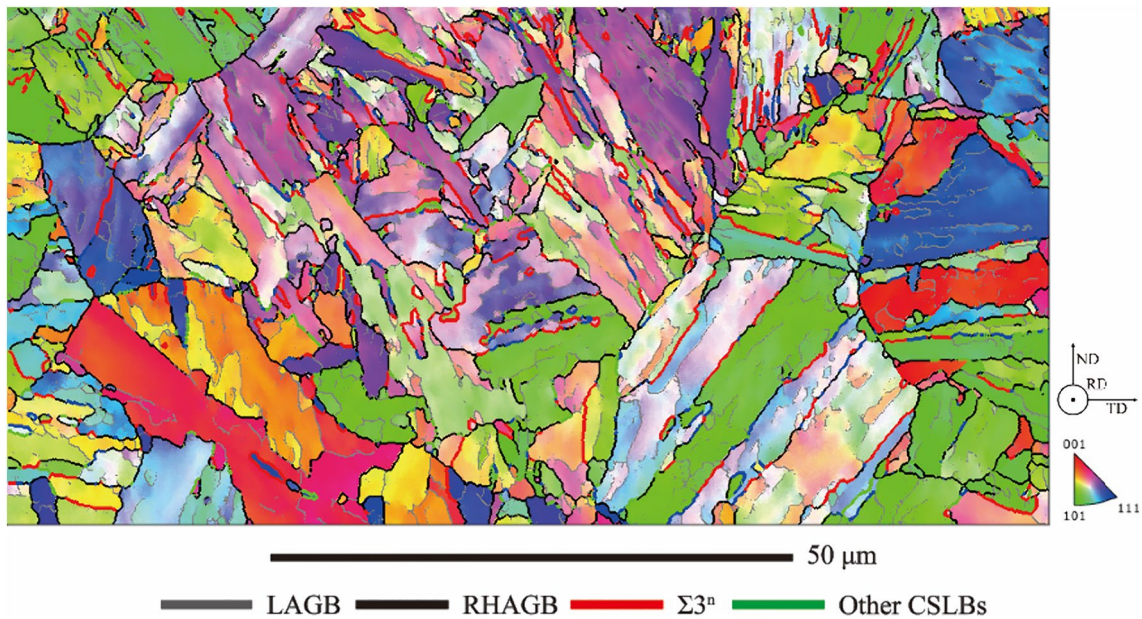


Fig. 2 (Color online) Inverse pole figure (IPF) map of the as-received (AR) specimen showing the character of individual grain boundaries in the martensite phase. Low angle grain boundaries (LAGBs), ran-

dom high angle grain boundaries (RHAGBs), $\Sigma 3^n$ boundaries, and other coincident site lattice boundaries (CSLBs) are indicated with grey, black, red, and green lines, respectively

were polished with sandpaper and wiped with anhydrous alcohol. The Tafel curve was measured in 0.03 M Na_2SO_4 and 0.03 M NaCl aqueous solution, which is consistent with the experimental environment of Pang et al. [35], at room temperature (RT) by utilizing the three-electrode system and CHI760e electrochemical workstation. The working electrode was the specimen, the reference electrode was a

saturated calomel electrode (SCE), and the auxiliary electrode was a platinum sheet. The experiment began when the steady-state open circuit potential (OCP) was reached, and the Tafel curve was obtained in the scanning range of -1 to 1 V with respect to the OCP at a scanning rate of 0.005 V/s. To ensure reproducibility, all the corrosion experiments were repeated at least three times.

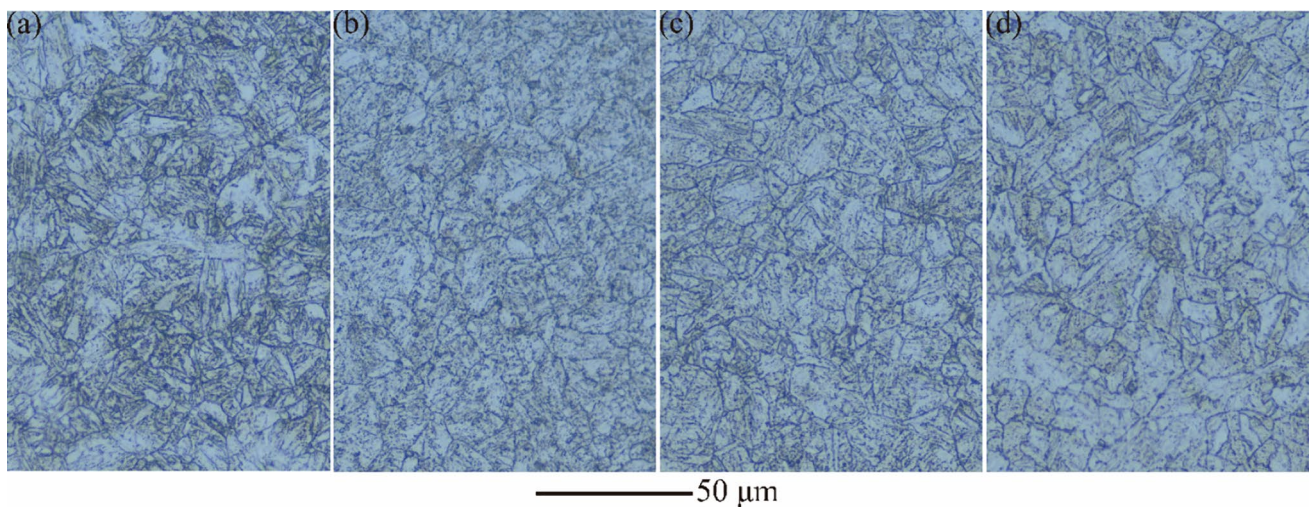


Fig. 3 Optical microscope images of the studied steels: **a** AR, **b** 6D, **c** 9D, **d** 12D

3 Results and discussion

3.1 Prior austenite grain size

The grain structures of TMP-treated P92 steel with different reduction ratios are shown in Fig. 3. For better visualization of the structure, the images were cropped to $250\ \mu\text{m} \times 220\ \mu\text{m}$. The distribution of the PAGBs and martensitic lath boundaries is shown in Fig. 3, indicating the typical microstructure of P92 steel.

Considering the thickness of specimens and the low cold-rolling reduction ratios, the PAG size was measured in two areas as shown in Fig. 4a, one just beneath the surface, identified as ‘edge’ and the other at the center of the specimen, identified as ‘middle’. Based on the metallographic analysis, the PAG sizes of the AR- and TMP-treated specimens against the reduction ratio are shown in Fig. 4a. Compared with the AR specimen, the PAG size of all TMP-treated specimens did not change significantly, which is consistent with the results in Ref. [18]; however, the PAG sizes of the specimens with different reduction ratios were slightly different. The PAG size in the edge area decreased with an increase in the reduction ratio, whereas the PAG size in the middle area increased with increasing cold-rolling reduction ratio, up to 9%, and then

decreased at a reduction ratio of 12%. The literature shows that the growth dynamics of the PAG are directly related to the degree of deformation, temperature, and time [50]. Under isothermal growth conditions, when the temperature is above the PAG growth temperature A_{c1} , the higher the peak temperature and the longer the holding time, the larger is the PAG size under ideal conditions. In this study, the normalizing temperature and normalizing time were the same, and the tempering temperature was lower than the PAG growth temperature. Therefore, the heat treatment process should have the same effect on the PAG size. In conclusion, the strain introduced by cold rolling was the only factor that affected the PAG size of the TMP-treated specimens. The recrystallization fraction determined by the grain orientation spread (GOS) value [51] was positively correlated with the reduction ratio in this study, as shown in Fig. 4b, indicating that the strain introduced by cold rolling promotes recrystallization. Only grains with $0^\circ < \text{GOS} < 1^\circ$ [52, 53] were identified as recrystallized grains, and this criterion was consistent with the experimental results. To the best of our knowledge, SIBM promotes grain growth, whereas recrystallization reduces the grain size [16, 29]. The relationship between the PAG size and recrystallization fraction calculated from the EBSD data in the edge area is consistent with the above discussion. However, this seems to contradict the changing trend

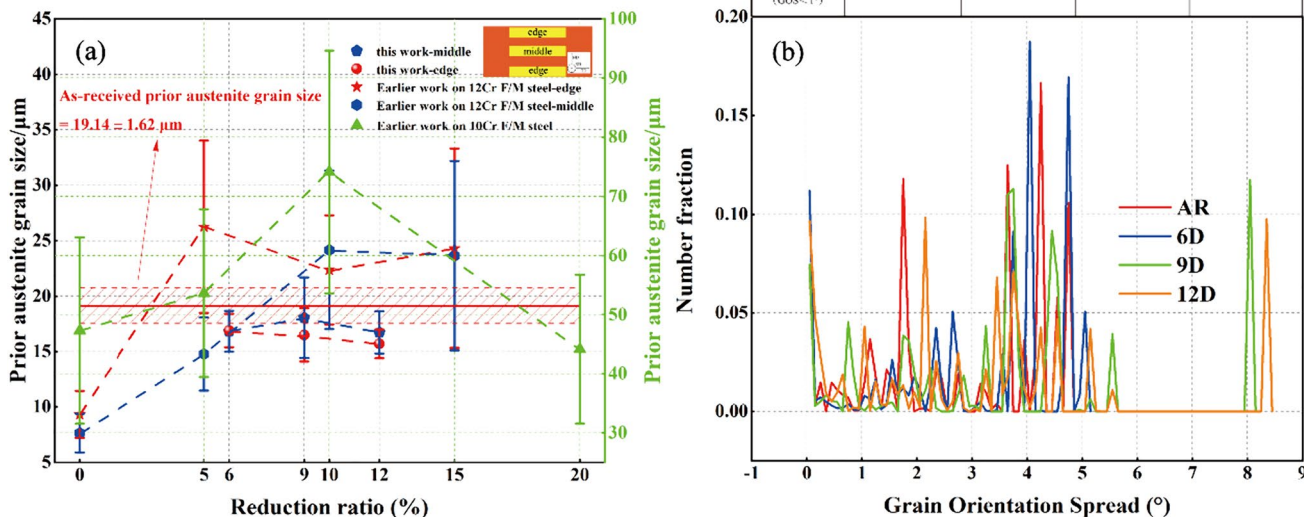


Fig. 4 (Color online) a prior austenite grain size of the studied steel under different thermomechanical processes (TMPs), b Grain orientation spread distribution for all the studied steels. The data on 10Cr

F/M steel and 12Cr F/M steel were extracted from Ref. [16] and Ref. [29], respectively

of the PAG size in the middle area. The following provides a detailed explanation of this contradiction. As shown in Fig. 4a, the edge and middle areas of 12Cr F/M steel also have different change trends in PAG size when the annealing time is 45 min. Kinoshita et al. [29] noted that a short time did not appear to be long enough for grain growth in the middle area when the reduction ratio was low. In our work, the variation trend of the PAG size in the middle area with the reduction ratio was inconsistent with that of

the recrystallization fraction because we collected EBSD data from the edge area.

Based on the above analysis, we can conclude that SIBM dominates at low strains, and recrystallization dominates as the strain increases. To the best of our knowledge, GB migration is usually accompanied by the formation of twins, and recrystallization usually introduces new random boundaries. Therefore, it can be expected that a high fraction of twin boundaries, corresponding to the {111} $\Sigma 3$ boundaries, will be introduced into the austenite phase for

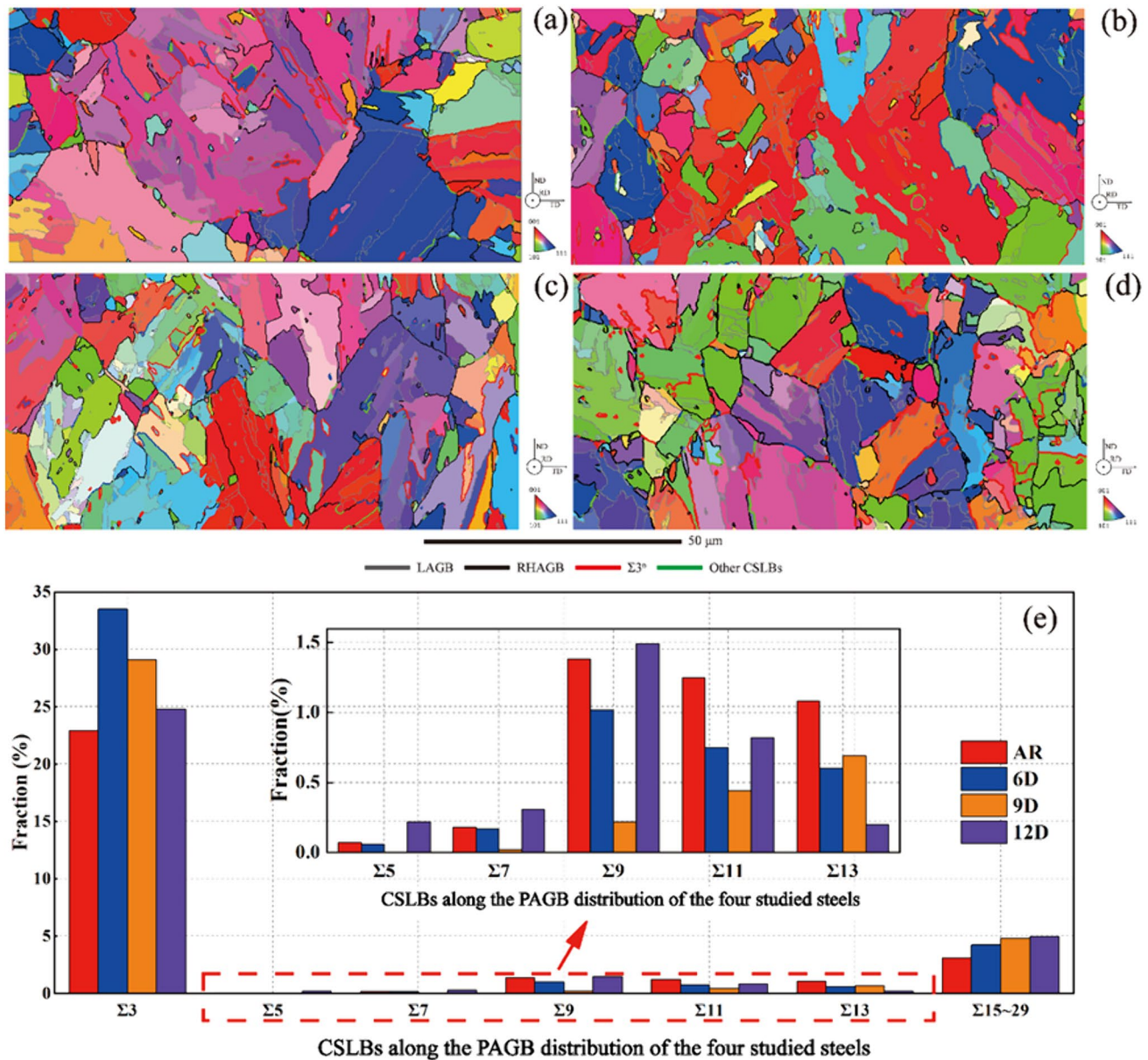


Fig. 5 (Color online) EBSD maps of P92 steel after prior austenite grain (PAG) reconstruction for the **a** AR, **b** 6D, **c** 9D, and **d** 12D specimens; **e** coincidence site lattice boundaries (CSLBs) along the distribution of prior austenite grain boundaries (PAGBs). The low

angle grain boundaries (LAGBs), random high angle grain boundaries (RHAGB), $\Sigma 3^n$, and other CSLBs are indicated with grey, black, red, and green lines, respectively

the 6D specimen, and the fraction of CSLBs along PAGBs will decrease with the increase in reduction ratio, which will be discussed in the next section.

3.2 Prior austenite grain boundary character distribution

The EBSD maps of AR specimen and the TMP-treated specimens after PAG reconstruction are shown in Fig. 5a–d. Different types of PAGBs are marked by rendering different colored line segments. For better visualization of the structure, the maps were cropped to $100\ \mu\text{m} \times 50\ \mu\text{m}$. Compared with the AR specimen as shown in Fig. 5a, it can be found that $\Sigma 3^n$ boundaries still account for the majority of CSLBs along the PAGBs after the TMP. To ensure statistical accuracy, at least 500 PAGBs were sampled for statistical analysis.

The fractions of CSLBs along the PAGBs of the studied steels are shown in Fig. 5e. The TMP clearly led to higher fractions of CSLBs along PAGBs. A high fraction of $\Sigma 3$ boundaries can be observed along PAGBs. Compared with the AR specimen, the fraction distribution of $\Sigma 3$ boundaries along PAGBs for 6D, 9D, and 12D improves by 46.3%, 27.1%, and 8.3%, respectively. Figure 6a shows the fraction of $\Sigma 3^n$ boundaries along PAGBs as a function of the reduction ratio for the AR specimen and TMP-treated specimens. The fraction of $\Sigma 3^n$ boundaries along PAGBs was evaluated as follows:

$$f_{(\Sigma 3^n)}^{(\gamma)} = \frac{L_{(\Sigma 3^n)}^{(\gamma)}}{L_{(\text{total})}^{(\gamma)}}, \quad (1)$$

where $L_{(\Sigma 3^n)}^{(\gamma)}$ is the total length of $\Sigma 3^n$ boundaries along PAGBs, and $L_{(\text{total})}^{(\gamma)}$ is the total length of PAGBs. The variation trend of the fraction of $\Sigma 3^n$ boundaries along PAGBs with the reduction is similar to that of PAG size. The fraction of $\Sigma 3^n$ boundaries along PAGBs decreases with the increasing reduction ratio. Figure 6b shows the relationship between the fraction of CSLBs along PAGBs and the reduction ratio. The fraction of CSLBs along PAGBs also decreased with an increasing reduction ratio. This finding is consistent with the results of Shimada et al. [11] and Kokawa et al. [22], who found a peak in the fraction of CSLBs at a 5% deformation and an inverse relationship between the fraction of CSLBs and the reduction ratio when the deformation was greater than 5% in γ -Fe. For comparison, the data obtained from 10 and 12Cr F/M steels are shown in Fig. 6a and the data obtained from 9 and 10Cr F/M steels are shown in Fig. 6b. As mentioned in Sect. 3.1, SIBM can promote twin formation, whereas recrystallization can introduce new random boundaries. However, the mechanism that dominates a given deformation is still unclear. We assume a special value of deformation, σ , for different materials and different TMPs. When the deformation is less than σ , SIBM is dominant, otherwise recrystallization is dominant instead of SIBM. Actually, σ is different for different materials and different TMPs. As can be observed from Fig. 6, σ is 10% in the work of Hirryama et al. (10Cr F/M steel) [16], and σ is 5% in the work of Kinoshita et al. (12Cr F/M steel) [29]. It can be reasonably guessed that the deformation was greater than σ

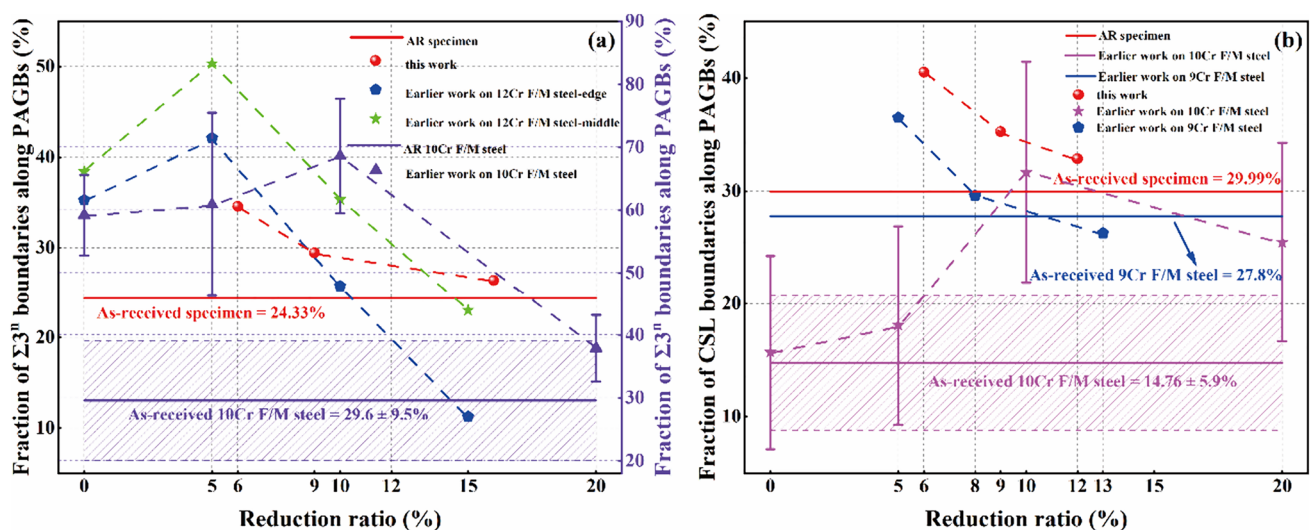


Fig. 6 (Color online) **a** Fraction of $\Sigma 3^n$ boundaries along PAGBs as a function of the reduction ratio, **b** relation between the fraction of CSLBs along PAGBs and the reduction ratio. The data on 9Cr F/M,

10Cr F/M, and 12Cr F/M steels were extracted from Ref. [17], Ref. [16], and Ref. [29], respectively. The shaded area represents the error bar

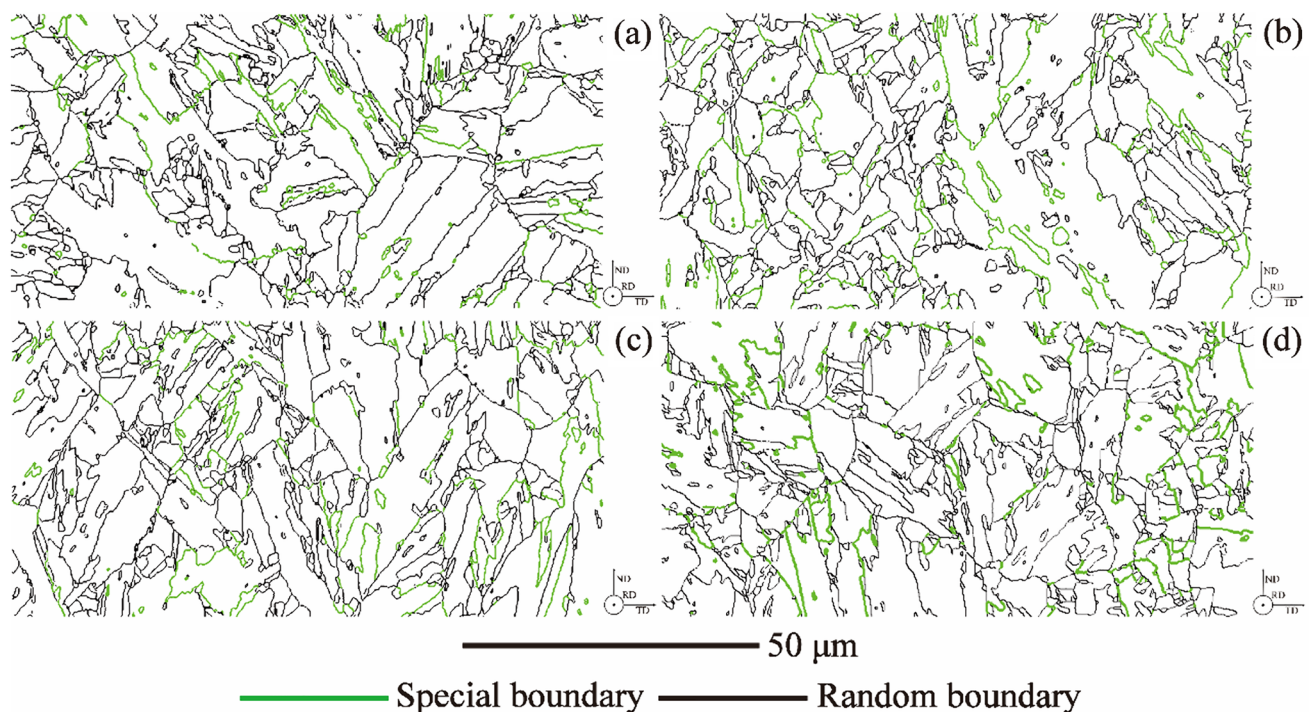


Fig. 7 (Color online) Schematic of the prior austenite grain boundary (PAGB) connectivity of the AR and TMP-treated specimens: **a** AR, **b** 6D, **c** 9D, **d** 12D

in this work, which can be confirmed from the recrystallization fraction in Sect. 3.1 and the change in trend of the fraction of $\Sigma 3^n$ boundaries along PAGBs and CSLBs along PAGBs.

3.3 Prior austenite grain boundary connectivity

Figure 7 shows the two-dimensional PAGB network of four steels, where the green and black lines denote special boundaries ($\Sigma 3$ – $\Sigma 29b$ boundaries) and random boundaries, respectively. Besides the different fraction of $\Sigma 3^n$ boundaries along PAGBs and CSLBs along PAGBs for the four studied steels, the distribution of special boundaries and the phenomena of reciprocal connectivity significantly vary. With the application of the cold-rolling–normalizing–tempering process, the random prior austenite GBs were segmented into fragments.

Percolation theory is typically used to simulate GB connectivity [54]. Previous studies suggested that four types of triple junctions can occur in a material [55]: TJ0 (R-R-R), TJ1 (S-R-R), TJ2 (S-S-R), and TJ3 (S-S-S), as shown in Fig. 8a. To assess GB connectivity, it is necessary to consider the distribution of triple junctions. To the best of our knowledge, a triple junction containing at least one random boundary is susceptible to such attacks. However, no TJ2 or TJ3 triple junctions were observed in any of the specimens, as shown in Fig. 8b. Only the 6D specimen had more TJ1 and fewer TJ0 triple junctions than the AR specimen.

The triple distributions of the other specimens were almost identical to those of the AR specimens. This means that only the 6D specimen has more broken prior austenite random boundaries than the AR specimen, whereas the other specimens show little change in prior austenite random boundary interruptions than the AR specimen.

3.4 Carbide particles

The SEM micrographs in Fig. 9 show the distribution of precipitates in the AR, 6D, 9D, and 12D specimens. One of the authors [56, 57] has proved that Cr-rich $M_{23}C_6$ is the main precipitate phase in P92 steel when tempering temperature is above 700 °C. To the best of our knowledge, subblock boundaries and PAGBs act as preferential nucleation sites for Cr-rich $M_{23}C_6$ and GBE can enhance the fraction of subblock boundaries [16, 17], leading to finely dispersed precipitates in the studied steel. Furthermore, CSLBs along the PAGBs can strongly suppress the formation and coarsening of chromium carbide precipitates, as mentioned in the Introduction, because the diffusivity of CSLBs is generally lower than that of random boundaries. A quantitative analysis of the precipitate phase requires further investigation, which is beyond the scope of this study. However, based on the above analysis, it can be inferred that the 6D, 9D, and 12D specimens have more densely dispersed precipitates than the AR specimens, as shown in Fig. 9, which is consistent with the results reported

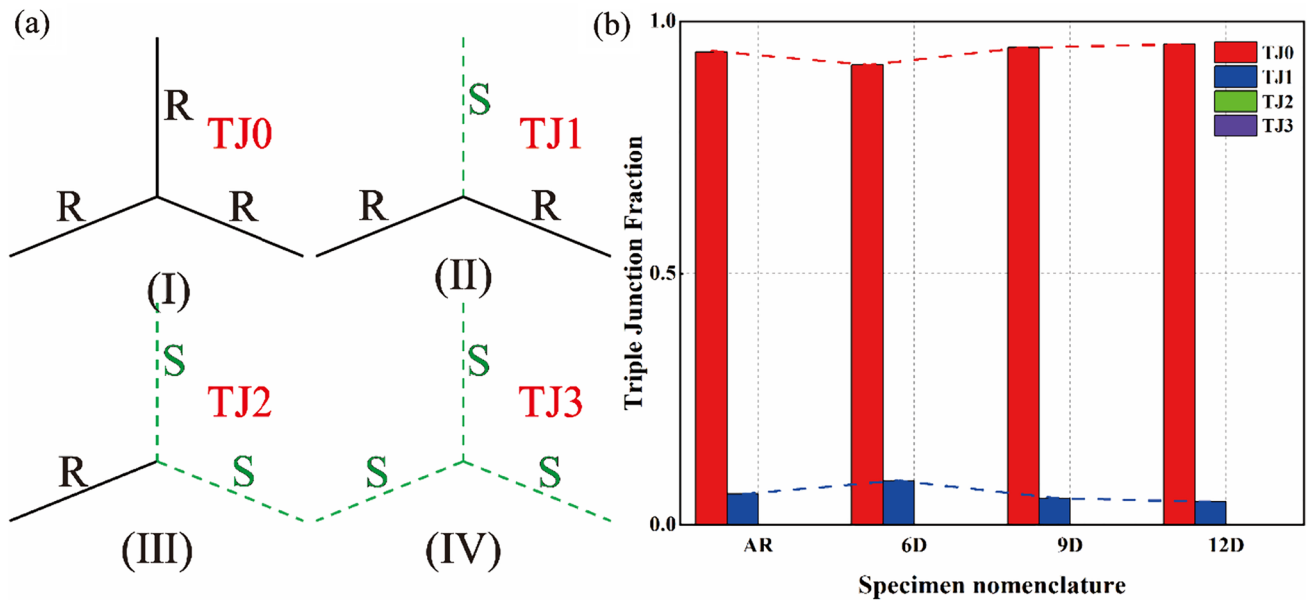


Fig. 8 (Color online) **a** Four types of triple junctions (S: special boundary, R: random boundary): (I) TJ0, (II) TJ1, (III) TJ2, (IV) TJ3; **b** triple junction distribution of the AR and TMP-treated specimens. The data was calculated by using Matlab software (mtx)

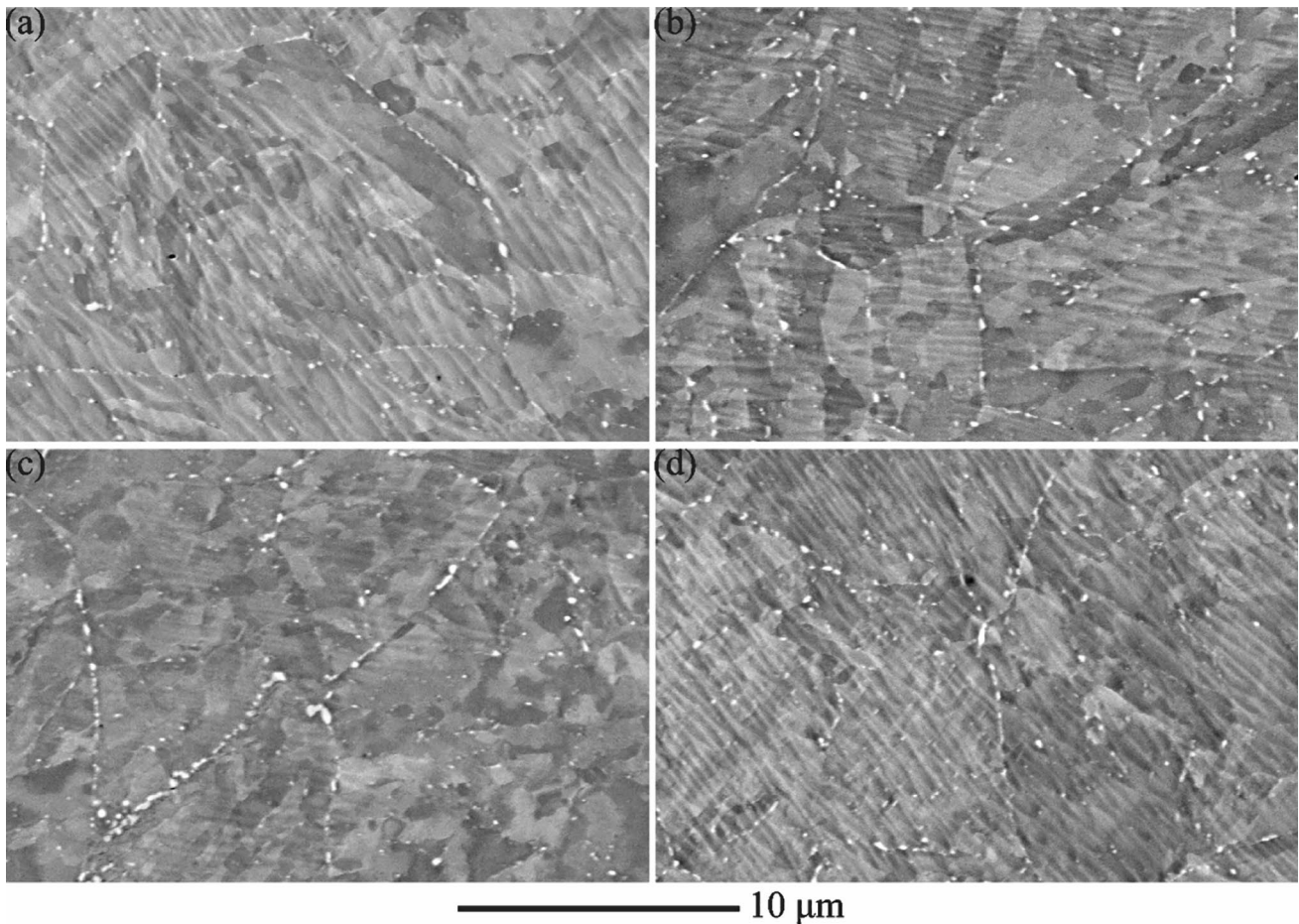


Fig. 9 SEM micrographs of the morphology of precipitation particles in **a** AR, **b** 6D, **c** 9D, and **d** 12D specimens

by Hirayama et al. [16] and Gupta et al. [18]. This means that the GBE-treated steel can achieve better high-temperature properties than the AR specimens. Experimental measurements of high-temperature properties will also be carried out in future studies. Meanwhile, it can also be inferred that the corrosion resistance will be improved in GBE-treated materials as chromium segregation is suppressed owing to the enhanced fraction of CSLBs along the PAGBs, as discussed in Sect. 3.2.

3.5 Corrosion behavior

The increase in CSLBs along the PAGBs fraction and the disruption of prior austenite random boundaries are helpful in improving the resistance to intergranular damage [16]. From the results of the analysis in Sects. 3.1, 3.2, and 3.3, a TMP with a low reduction ratio can enhance the fraction of CSLBs along the PAGBs and disrupt the prior austenite random boundaries, thereby improving the intergranular resistance. In this study, electrochemical corrosion tests were conducted to determine whether these changes in the prior austenite GBCD and PAGB connectivity are associated with corrosion resistance. All the corrosion tests were repeated at least three times, and representative data are presented.

Potentiodynamic polarization curves were measured to determine the self-corrosion density (i_{corr}) and self-corrosion rate (v), as shown in Fig. 10a, and to verify the effectiveness of the GBE. i_{corr} was obtained by extrapolating the potentiodynamic polarization curve, and v was calculated according to the following formula [58]:

$$v = \frac{M}{nF} i_{\text{corr}}, \quad (2)$$

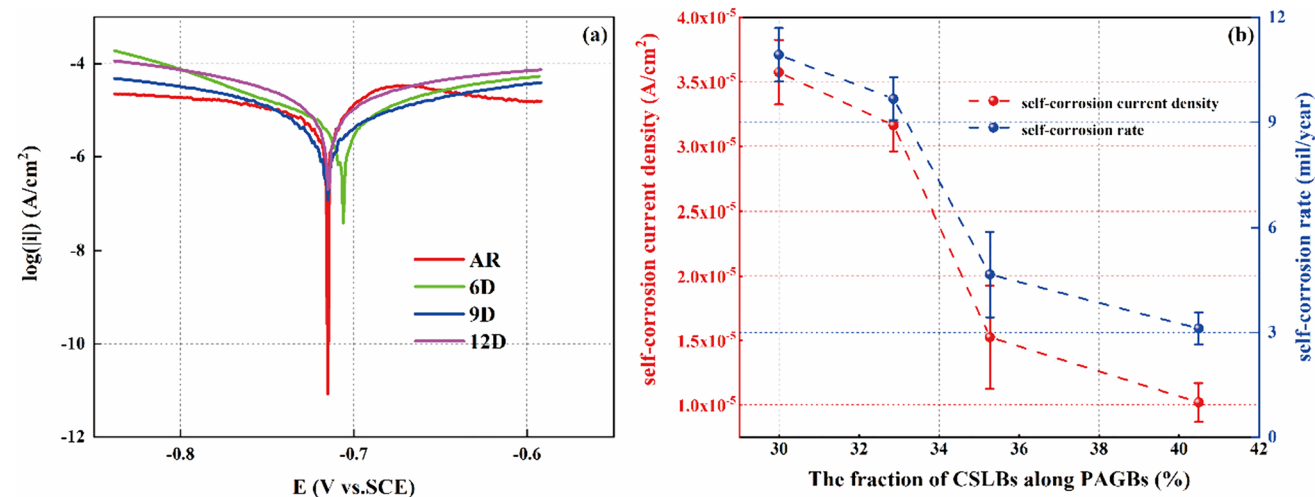


Fig. 10 (Color online) **a** Potentiodynamic polarization curves, **b** self-corrosion current density and self-corrosion rate as a function of the fraction of CSLBs along PAGBs

Table 2 Extraction of character values of potentiodynamic polarization curves

Specimen nomenclature	i_{corr} (A/cm ²)	v (mil/year)
AR	$(3.57 \pm 0.25) \times 10^{-5}$	10.92 ± 0.74
6D	$(1.02 \pm 0.15) \times 10^{-5}$	3.12 ± 0.46
9D	$(1.53 \pm 0.41) \times 10^{-5}$	4.66 ± 1.25
12D	$(3.16 \pm 0.19) \times 10^{-5}$	9.66 ± 0.58

where M is the molecular mass of the material, n is the number of shifted electrons, and F is Faraday's constant. The corresponding data are listed in Table 2.

The variations of i_{corr} , as well as corrosion rate v followed a trend contrary to the change in the fraction of CSLBs along PAGBs, as shown in Fig. 10b. As the fraction of CSLBs along PAGBs increases, the value of i_{corr} is $(1.02 \pm 0.15) \times 10^{-5}$, $(1.53 \pm 0.41) \times 10^{-5}$, $(3.16 \pm 0.19) \times 10^{-5}$, and $(3.57 \pm 0.25) \times 10^{-5}$ A·cm⁻², respectively, and the value of v is 3.12 ± 0.46 , 4.66 ± 1.25 , 9.66 ± 0.58 , 10.92 ± 0.74 mil·year⁻¹, respectively. The self-corrosion density and rate of the TMP-treated specimens were lower than those of the AR specimen, reflecting an improvement in the electrochemical corrosion resistance. The specimen with more CSLBs along PAGBs showed a decreasing electrochemical corrosion susceptibility, which proves that GBE is effective in improving the intergranular damage resistance of P92 steel under the presented conditions. In addition, this result is in accordance with the visual inspection of the metallographic analysis.

Typical SEM micrographs of AR and TMP-treated specimens after the potentiodynamic polarization test in 0.03 M

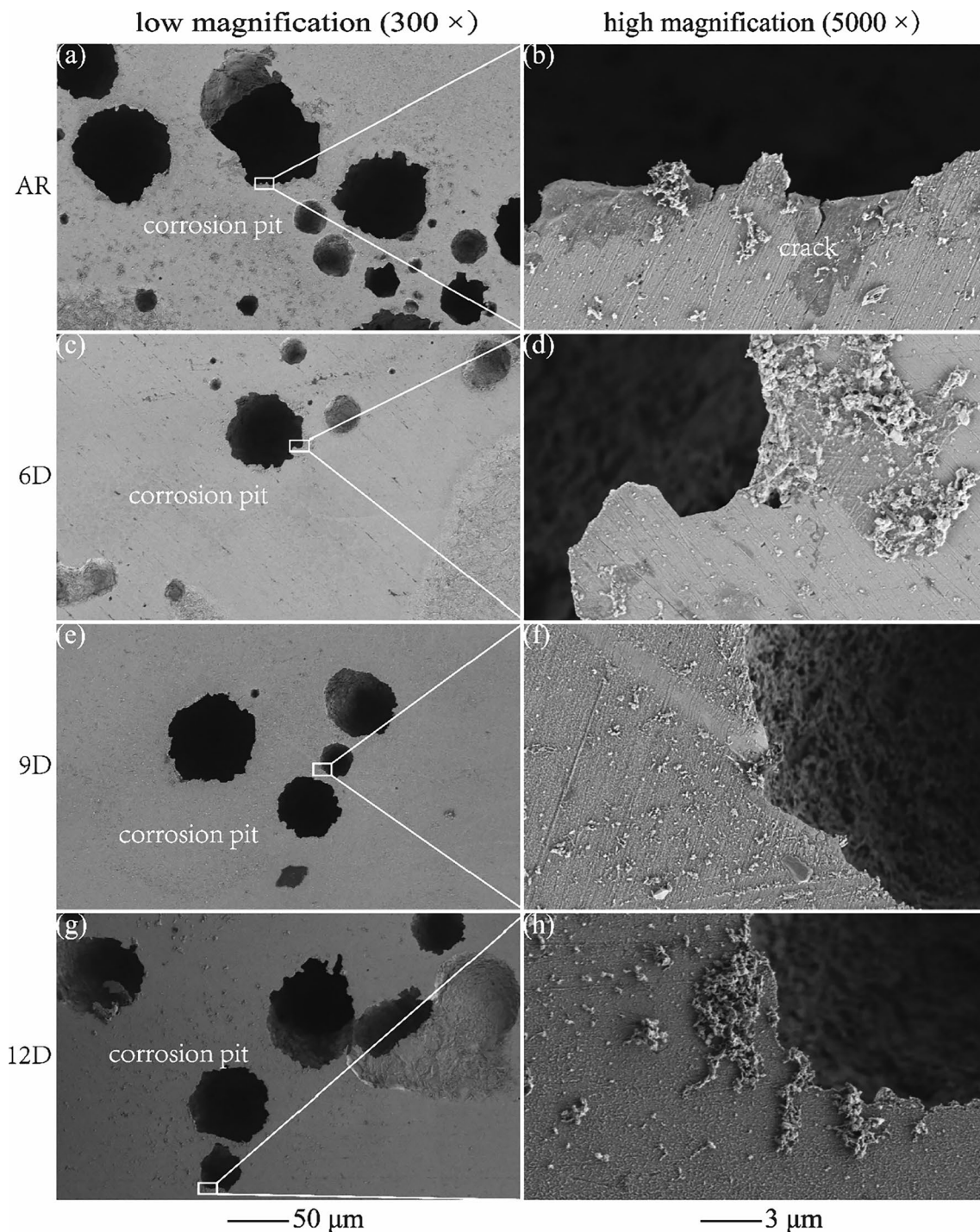


Fig. 11 SEM micrographs of the specimens after anodic polarization. Low magnification for **a** AR, **c** 6D, **e** 9D, and **g** 12D. High magnification for **b** AR, **d** 6D, **f** 9D, and **h** 12D

Na_2SO_4 and 0.03 M NaCl aqueous solutions are shown in Fig. 11a–h. The electrochemical corrosion morphologies of the AR specimens show larger and denser corrosion pits than those of the TMP-treated specimens. In addition, the high-magnification micrograph of the AR specimen indicates that corrosion cracks were generated, as shown in Fig. 11b,

which were not observed in the other specimens, as shown in Fig. 11d, f, h. The electrochemical corrosion morphologies of the 9D and 12D specimens show fewer corrosion pits than those of the AR specimen, as shown in Fig. 11e–h, and their surfaces are smoother than those of the AR specimen. The electrochemical corrosion morphologies of the 6D

specimen exhibited the lowest number of corrosion pits and demonstrated a low degree of corrosion compared with the other specimens, as shown in Fig. 11c, d.

4 Conclusion

Through metallographic analysis and EBSD tests, the PAG size, prior austenite GBCD, and prior austenite grain boundary connectivity of F/M steel P92 under different TMPs were explored. Electrochemical corrosion tests were performed to verify the validity of GBE. The major findings of this study are as follows:

The PAG size of all the TMP-treated specimens did not change significantly compared with that of the AR specimen. The PAG size decreased with increasing reduction ratio in the edge area owing to the increasing recrystallization fraction. The PAG size increased with a deformation of up to 9% and then decreased in the middle area because the normalizing time was short.

Different special values of deformation, σ , were found for different materials and different TMPs. When the deformation was lower than σ , SIBM is dominant, otherwise recrystallization is dominant. In this work, the fraction of CSLBs along PAGBs decreased with increasing reduction ratio because the deformation was greater than σ .

Potentiodynamic polarization studies revealed that the electrochemical corrosion resistance of P92 steel can be improved by introducing a high fraction of CSLBs along PAGBs under the presented conditions. Therefore, the GBE method is feasible and effective for improving the intergranular damage resistance of F/M steels.

Acknowledgements The authors thank Ye Cheng, a former student from Shanghai Jiao Tong University, for assistance with the thermo-mechanical processes. The authors also thank Prof. Aidang Shan of Shanghai Jiao Tong University for supplying the experimental steel. The authors also acknowledge the Engineering and Material Sciences Department, University of Science and Technology of China (USTC), and the Instrumental Analysis Center, Shanghai Jiao Tong University (SJTU).

Author contributions All authors contributed to the study conception and design. Material preparation, data collection and analysis were performed by LP, S-MC, J-YS, Y-ZS and H-JW. The first draft of the manuscript was written by LP, S-MC, and J-YS, and all authors commented on previous versions of the manuscript. All authors read and approved the final manuscript.

Data availability The data that support the findings of this study are openly available in Science Data Bank at <https://cstr.cn/31253.11.sciencedb.j00186.00379> and <https://doi.org/10.57760/sciencedb.j00186.00379>.

Declarations

Conflict of interest The authors declare that they have no competing interests.

References

1. N. Saini, C. Pandey, M.M. Mahapatra, Characterization and evaluation of mechanical properties of CSEF P92 steel for varying normalizing temperature. *Mater. Sci. Eng. A* **688**, 250–261 (2017). <https://doi.org/10.1016/j.msea.2017.02.022>
2. X.G. Tao, J.F. Gu, L.Z. Han, Characterization of precipitates in X12CrMoWVNbN10-1-1 steel during heat treatment. *J. Nucl. Mater.* **452**, 557–564 (2014). <https://doi.org/10.1016/j.jnucmat.2014.06.018>
3. L. Maddi, A.R. Ballal, D.R. Peshwe et al., Effect of tempering temperature on the stress rupture properties of Grade 92 steel. *Mater. Sci. Eng. A* **639**, 431–438 (2015). <https://doi.org/10.1016/j.msea.2015.05.062>
4. D.D. Zhao, S.L. Li, Y.L. Wang et al., Investigation of ion irradiation hardening behaviors of tempered and long-term thermal aged T92 steel. *J. Nucl. Mater.* **511**, 191–199 (2018). <https://doi.org/10.1016/j.jnucmat.2018.09.016>
5. H.Y. He, Y.Z. Shen, Y.J. Guo, Precipitates change of P92 steel under 3.5 MeV Fe¹³⁺ ion irradiation at 400 °C. *Mater. Charact.* **205**, 113273 (2023). <https://doi.org/10.1016/j.matchar.2023.113273>
6. Q.D. Chen, F.H. Gao, Establishment and verification of chemical interaction model between fast reactor fuel and cladding under high burnup. *Nucl. Tech. (in Chinese)* **45**, 80–86 (2022). <https://doi.org/10.11889/j.0253-3219.2022.hjs.45.010603>
7. L. Tan, M.A. Sokolov, S.J. Pawel et al., Varied enhancements in mechanical properties and sodium compatibility of Grade 92 by thermomechanical treatments. *Mater. Sci. Eng. A* **832**, 142359 (2022). <https://doi.org/10.1016/j.msea.2021.142359>
8. X. Jin, B.Y. Zhu, Y.F. Li et al., Effect of the microstructure evolution on the high-temperature strength of P92 heat-resistant steel for different service times. *Int. J. Press. Vessels Pip.* **186**, 104131 (2020). <https://doi.org/10.1016/j.ijpvp.2020.104131>
9. Z. Zhang, Z.F. Hu, L.F. Zhang et al., Effect of temperature and dissolved oxygen on stress corrosion cracking behavior of P92 ferritic-martensitic steel in supercritical water environment. *J. Nucl. Mater.* **498**, 89–102 (2018). <https://doi.org/10.1016/j.jnucmat.2017.10.024>
10. E.I. Samuel, B.K. Choudhary, D.P.R. Palaparti et al., Creep deformation and rupture behaviour of P92 steel at 923 K. *Procedia Eng.* **55**, 64–69 (2013). <https://doi.org/10.1016/j.proeng.2013.03.220>
11. M. Shimada, H. Kokawa, Z.J. Wang et al., Optimization of grain boundary character distribution for intergranular corrosion resistant 304 stainless steel by twin-induced grain boundary engineering. *Acta Mater.* **50**, 2331–2341 (2002). [https://doi.org/10.1016/S1359-6454\(02\)00064-2](https://doi.org/10.1016/S1359-6454(02)00064-2)
12. J.H. Zhang, K. Hu, J.Y. Zhao et al., Effect of heat input on microstructure and corrosion resistance in heat affected zone of 304 stainless steel joint by laser welding. *Mater. Today Commun.* **30**, 103054 (2022). <https://doi.org/10.1016/j.mtcomm.2021.103054>
13. Y. Zhou, K.T. Aust, U. Erb et al., Effects of grain boundary structure on carbide precipitation in 304L stainless steel. *Scr. Mater.* **45**, 49–54 (2001). [https://doi.org/10.1016/S1359-6462\(01\)00990-3](https://doi.org/10.1016/S1359-6462(01)00990-3)
14. V. Randle, Twinning-related grain boundary engineering. *Acta Mater.* **52**, 4067–4081 (2004). <https://doi.org/10.1016/j.actamat.2004.05.031>
15. T. Watanabe, S. Tsurekawa, Toughening of brittle materials by grain boundary engineering. *Mater. Sci. Eng. A* **387–389**, 447–455 (2004). <https://doi.org/10.1016/j.msea.2004.01.140>
16. K. Hirayama, Y. Yoshii, Y. Morizono et al., Grain boundary engineering of 10% Cr ferritic-martensitic steel SUH3. *ISIJ Int.* **55**, 1973–1979 (2015). <https://doi.org/10.2355/isijinternational.isijnt-2015-057>

17. G. Gupta, G.S. Was, B. Alexandreanu, Grain boundary engineering of ferritic-martensitic alloy T91. *Metall. Mater. Trans. A* **35**, 717–719 (2004). <https://doi.org/10.1007/s11661-004-0382-3>
18. G. Gupta, P. Ampornrat, X. Ren et al., Role of grain boundary engineering in the SCC behavior of ferritic–martensitic alloy HT-9. *J. Nucl. Mater.* **361**, 160–173 (2007). <https://doi.org/10.1016/j.jnucmat.2006.12.006>
19. Z. Fan, Y.D. Zhang, X.G. Hu et al., Effect of grain boundary engineering on corrosion behavior of nickel-based alloy 825 in sulfur environment. *Mater. Res. Express* **8**, 066530 (2021). <https://doi.org/10.1088/2053-1591/ac0cc5>
20. E.S. Huron, K.R. Bain, D.P. Mourer et al., The influence of grain boundary elements on properties and microstructures of P/M nickel base superalloys, in *Proc.* ed. by K.A. Green, T.M. Pollock, H. Harada, T.E. Howson, R.C. Reed, J.J. Schirra, S. Walston (Int. Symp. Superalloys, 2004), pp.73–81. https://doi.org/10.7449/2004/superalloys_2004_73_81
21. T.G. Liu, S. Xia, H. Li et al., Effect of the pre-existing carbides on the grain boundary network during grain boundary engineering in a nickel based alloy. *Mater Charact* **91**, 89–100 (2014). <https://doi.org/10.1016/j.matchar.2014.02.011>
22. H. Kokawa, W.Z. Jin, Z.J. Wang et al., Grain boundary engineering of high-nitrogen austenitic stainless steel. *Mater. Sci. Forum* **539–543**, 4962–4967 (2007). <https://doi.org/10.4028/0-87849-428-6.4962>
23. W.Z. Jin, H. Kokawa, Z.J. Wang et al., Improvement of transpassive intergranular corrosion resistance of 304 austenitic stainless steel by thermomechanical processing for twin-induced grain boundary engineering. *ISIJ Int.* **50**, 476–481 (2010). <https://doi.org/10.2355/isijinternational.50.476>
24. H. Kokawa, Potential of grain boundary engineering to suppress welding degradations of austenitic stainless steels. *Sci. Technol. Weld. Join.* **16**, 357–362 (2011). <https://doi.org/10.1179/1362171811y.0000000021>
25. S. Tokita, H. Kokawa, S. Kodama et al., Suppression of intergranular corrosion by surface grain boundary engineering of 304 austenitic stainless steel using laser peening plus annealing. *Mater. Today Commun.* **25**, 101572 (2020). <https://doi.org/10.1016/j.mtcomm.2020.101572>
26. F. Shi, X.W. Li, Y.T. Hu et al., Optimization of grain boundary character distribution in Fe-18Cr-18Mn-0.63N high-nitrogen austenitic stainless steel. *Acta Metall. Sin. Engl. Lett.* **26**, 497–502 (2013). <https://doi.org/10.1007/s40195-013-0323-5>
27. Z.Q. Wang, H.H. Wu, Y. Wu et al., Solving oxygen embrittlement of refractory high-entropy alloy via grain boundary engineering. *Mater. Today* **54**, 83–89 (2022). <https://doi.org/10.1016/j.mattod.2022.02.006>
28. F.H. Cao, Y. Chen, S.T. Zhao et al., Grain boundary phase transformation in a CrCoNi complex concentrated alloy. *Acta Mater.* **209**, 116786 (2021). <https://doi.org/10.1016/j.actamat.2021.116786>
29. Y. Kinoshita, V.A. Yardley, S. Tsurekawa, Relation between microstructures of martensite and prior austenite in 12 wt% Cr ferritic steel. *J. Mater. Sci.* **46**, 4261–4269 (2011). <https://doi.org/10.1007/s10853-010-5241-6>
30. V.S. Saji, Superhydrophobic surfaces and coatings by electrochemical methods—a review. *J. Adhes. Sci. Technol.* **37**, 137–161 (2023). <https://doi.org/10.1080/01694243.2022.2031462>
31. F. Mansfeld, B. Little, A technical review of electrochemical techniques applied to microbiologically influenced corrosion. *Corros. Sci.* **32**, 247–272 (1991). [https://doi.org/10.1016/0010-938X\(91\)90072-W](https://doi.org/10.1016/0010-938X(91)90072-W)
32. Y. Zou, J. Wang, Y.Y. Zheng, Electrochemical techniques for determining corrosion rate of rusted steel in seawater. *Corros. Sci.* **53**, 208–216 (2011). <https://doi.org/10.1016/j.corsci.2010.09.011>
33. H.M. Zhang, L. Yan, Y.Y. Zhu et al., The effect of immersion corrosion time on electrochemical corrosion behavior and the corrosion mechanism of EH47 ship steel in seawater. *Metals* **11**, 1317 (2021). <https://doi.org/10.3390/met11081317>
34. K. Azumi, M. Seo, Corrosion behavior of titanium-clad carbon steel in weakly alkaline solutions. *Corros. Sci.* **45**, 413–426 (2003). [https://doi.org/10.1016/S0010-938X\(02\)00124-5](https://doi.org/10.1016/S0010-938X(02)00124-5)
35. F.F. Pang, *Study on corrosion behavior of T/P92 heat-resistant steel* (Changsha University of Science & Technology, Dissertaion, 2014)
36. Y.Z. Shen, H. Liu, Z.X. Shang et al., Precipitate phases in normalized and tempered ferritic/martensitic steel P92. *J. Nucl. Mater.* **465**, 373–382 (2015). <https://doi.org/10.1016/j.jnucmat.2015.05.043>
37. Y.Z. Shen, B. Ji, X.L. Zhou, M5C2 carbide precipitates in a high-Cr martensitic steel. *Met. Mater. Int.* **20**, 503–506 (2014). <https://doi.org/10.1007/s12540-014-3014-5>
38. Y.Z. Shen, X.L. Zhou, Z.X. Shang, Neodymium-rich precipitate phases in a high-chromium ferritic/martensitic steel. *Met. Mater. Int.* **22**, 459–467 (2016). <https://doi.org/10.1007/s12540-016-5696-3>
39. Z.Q. Xu, Y.Z. Shen, Z.X. Shang et al., Precipitate phases in ferritic/martensitic steel P92 after thermomechanical treatment. *J. Nucl. Mater.* **509**, 355–365 (2018). <https://doi.org/10.1016/j.jnucmat.2018.04.025>
40. G. Dak, C. Pandey, Experimental investigation on microstructure, mechanical properties, and residual stresses of dissimilar welded joint of martensitic P92 and AISI 304L austenitic stainless steel. *Int. J. Press. Vessels Pip.* **194**, 104536 (2021). <https://doi.org/10.1016/j.ijpvp.2021.104536>
41. V. Maduraimuthu, P. Vasantharaja, M. Vasudevan et al., Microstructure and mechanical properties of 9Cr-0.5Mo-1.8W-VNb (P92) steel weld joints processed by fusion welding. *Mater. Sci. Eng. A* **813**, 141186 (2021). <https://doi.org/10.1016/j.msea.2021.141186>
42. G. Sharma, D.K. Dwivedi, Study of metallurgical and mechanical properties of CSEF P92 steel diffusion bonds developed using pressure pulsation. *J. Manuf. Process.* **38**, 196–203 (2019). <https://doi.org/10.1016/j.jmapro.2019.01.017>
43. D. Rath, P. Setia, N. Tripathi et al., Outstanding improvement in the CSL distribution in interstitial free (IF) steel via strain annealing route. *Mater Charact* **186**, 111817 (2022). <https://doi.org/10.1016/j.matchar.2022.111817>
44. D.G. Brandon, The structure of high-angle grain boundaries. *Acta Metall.* **14**, 1479–1484 (1966). [https://doi.org/10.1016/0001-6160\(66\)90168-4](https://doi.org/10.1016/0001-6160(66)90168-4)
45. C. Cayron, B. Artaud, L. Briottet, Reconstruction of parent grains from EBSD data. *Mater Charact* **57**, 386–401 (2006). <https://doi.org/10.1016/j.matchar.2006.03.008>
46. K. Zhang, X.B. Liu, L. Zhu, Characterisation of microstructure evolution during creep of P91 steel using the electron backscatter diffraction technique. *Mater. High Temp.* **38**, 158–165 (2021). <https://doi.org/10.1080/09603409.2021.1897941>
47. A. Brust, E. Payton, T. Hobbs et al., Probabilistic reconstruction of austenite microstructure from electron backscatter diffraction observations of martensite. *Microsc. Microanal.* **27**, 1035–1055 (2021). <https://doi.org/10.1017/s1431927621012484>
48. C.Y. Huang, H.C. Ni, H.W. Yen, New protocol for orientation reconstruction from martensite to austenite in steels. *Materialia* **9**, 100554 (2020). <https://doi.org/10.1016/j.mtla.2019.100554>
49. T. Sakthivel, G. Sasikala, M.K. Dash et al., Creep deformation and rupture behavior of P92 steel weld joint fabricated by NG-TIG welding process. *J. Mater. Eng. Perform.* **28**, 4364–4378 (2019). <https://doi.org/10.1007/s11665-019-04157-1>
50. J.C. Wang, P.L. Nie, S.F. Qiao et al., Investigation on microstructural evolutions and mechanical properties of P92 steel during

- thermal processing. *J. Mater. Eng. Perform.* **27**, 4392–4404 (2018). <https://doi.org/10.1007/s11665-018-3562-9>
51. D.K. Guan, X.G. Liu, J.H. Gao et al., Exploring the mechanism of “Rare Earth” texture evolution in a lean Mg–Zn–Ca alloy. *Sci. Rep.* **9**, 7152 (2019). <https://doi.org/10.1038/s41598-019-43415-z>
 52. I. Basu, T. Al-Samman, Twin recrystallization mechanisms in magnesium-rare earth alloys. *Acta Mater.* **96**, 111–132 (2015). <https://doi.org/10.1016/j.actamat.2015.05.044>
 53. K. Hantzsche, J. Bohlen, J. Wendt et al., Effect of rare earth additions on microstructure and texture development of magnesium alloy sheets. *Scr. Mater.* **63**, 725–730 (2010). <https://doi.org/10.1016/j.scriptamat.2009.12.033>
 54. J. Han, H.J. Li, Z.X. Zhu et al., Effects of processing optimisation on microstructure, texture, grain boundary and mechanical properties of Fe–17Cr ferritic stainless steel thick plates. *Mater. Sci. Eng. A* **616**, 20–28 (2014). <https://doi.org/10.1016/j.msea.2014.07.107>
 55. P. Fortier, W.A. Miller, K.T. Aust, Triple junction and grain boundary character distributions in metallic materials. *Acta Mater.* **45**, 3459–3467 (1997). [https://doi.org/10.1016/S1359-6454\(97\)00004-9](https://doi.org/10.1016/S1359-6454(97)00004-9)
 56. Z.J. Fan, Y.Z. Shen, Z.Q. Xu et al., Evolution of precipitate phases in ferritic and martensitic steel P92 during normalizing and tempering. *JOM* **74**, 3578–3594 (2022). <https://doi.org/10.1007/s11837-022-05272-6>
 57. S.Z. Li, Z. Eliniyaz, F. Sun et al., Effect of thermo-mechanical treatment on microstructure and mechanical properties of P92 heat resistant steel. *Mater. Sci. Eng. A* **559**, 882–888 (2013). <https://doi.org/10.1016/j.msea.2012.09.040>
 58. P.Y. Lun, Z.H. Lu, X.G. Zhang et al., Experimental study and suggested mathematical model for chloride-induced reinforcement corrosion rate. *Structures* **34**, 2014–2029 (2021). <https://doi.org/10.1016/j.istruc.2021.08.099>

Springer Nature or its licensor (e.g. a society or other partner) holds exclusive rights to this article under a publishing agreement with the author(s) or other rightsholder(s); author self-archiving of the accepted manuscript version of this article is solely governed by the terms of such publishing agreement and applicable law.

Authors and Affiliations

Lei Peng^{1,2} · Shang-Ming Chen^{1,2}  · Jing-Yi Shi^{1,2}  · Yong-Jie Sun^{1,2} · Yi-Fei Liu^{1,2} · Yin-Zhong Shen³ · Hong-Ya He³ · Hui-Juan Wang⁴ · Jie Tian⁴

✉ Jing-Yi Shi
shijy@ustc.edu.cn

✉ Yin-Zhong Shen
shenyz@sues.edu.cn

¹ State Key Laboratory of Particle Detection and Electronics, University of Science and Technology of China, Hefei 230026, China

² School of Nuclear Science and Technology, University of Science and Technology of China, Hefei 230027, China

³ School of Materials Engineering, Shanghai University of Engineering Science, 333 Long Teng Road, Shanghai 201620, China

⁴ Experimental Center of Engineering and Material Science, University of Science and Technology of China, Hefei 230026, China